ATMOSPHERIC SCIENCE

Large diurnal compensatory effects mitigate the response of Amazonian forests to atmospheric warming and drying

Zhaoying Zhang[1,2,3], Alessandro Cescatti[4], Ying-Ping Wang[5], Pierre Gentine[6], Jingfeng Xiao[7], Luis Guanter[8], Alfredo R. Huete[9], Jin Wu[10,11], Jing M. Chen[12], Weimin Ju[1,3], Josep Peñuelas[13,14], Yongguang Zhang[1,3,15]*

Photosynthesis and evapotranspiration in Amazonian forests are major contributors to the global carbon and water cycles. However, their diurnal patterns and responses to atmospheric warming and drying at regional scale remain unclear, hindering the understanding of global carbon and water cycles. Here, we used proxies of photosynthesis and evapotranspiration from the International Space Station to reveal a strong depression of dry season afternoon photosynthesis (by 6.7 ± 2.4%) and evapotranspiration (by 6.1 ± 3.1%). Photosynthesis positively responds to vapor pressure deficit (VPD) in the morning, but negatively in the afternoon. Furthermore, we projected that the regionally depressed afternoon photosynthesis will be compensated by their increases in the morning in future dry seasons. These results shed new light on the complex interplay of climate with carbon and water fluxes in Amazonian forests and provide evidence on the emerging environmental constraints of primary productivity that may improve the robustness of future projections.

INTRODUCTION

Amazonian rainforests play an important role in the climate system by exchanging large amounts of energy, water, and carbon dioxide (CO_2) with the atmosphere and acting as a major carbon stock. Climate change is expected to make the Amazon forest substantially warmer and potentially drier over the 21st century (*1*) with potential warring impacts on primary productivity and the regional carbon budget. Photosynthesis and evapotranspiration (ET) may decline under future atmospheric warming and drying due to the stomatal closure, hydraulic failure, and Rubisco enzymatic capacity impairment (*2*, *3*). Large-scale decreases in ET might further feed back to the regional climate by reducing cloud formation and subsequent rainfall events (*4*), causing a higher risk of drought and tree mortality (*5*). Moreover, the negative impact on primary productivity of Amazon forests could substantially weaken their carbon uptake (*6*).

Given these potential climate impacts on Amazon rainforests, it is becoming critical to understand and predict the direction and magnitude of photosynthesis and ET changes in response to atmospheric warming and drying in Amazonian forests (*7*, *8*). Dynamic global vegetation models were used to predict forest response to long-term climate change, whereas there were substantial uncertainties in the prediction due to their poor responses to short-term variations in environmental drivers (*9*). For example, because land-surface models do not accurately account for the daily hysteretic response of stomatal conductance to compound atmospheric and soil dryness, most of them underestimate and overestimate latent heat flux (LE; equivalent to ET) in the morning and afternoon, respectively (*10*). These mechanisms also highlight difficulties in predicting the responses of photosynthesis and transpiration to warmer and drier conditions.

In addition to model simulations, numerous studies based on ground and satellite measurements have quantified the underlying mechanisms (biotic or abiotic) of the Amazon seasonality (*11*–*13*). The photosynthetic seasonality in Amazonian forests is strongly related to phenology (that is, leaf development and demography) (*11*), rather than directly to the physiological response to environmental drivers that explain only 3% of the photosynthesis variability at the monthly scale (*14*). As a result, the response of Amazonian forests to atmospheric warming and drying remains controversial, because conventional assessments of these environmental effects on photosynthesis and ET, such as the changes in the phenology of leaves and their age demography (young or mature) at seasonal scale, often masked out their responses to warming or drying at the diurnal time scale.

Nevertheless, environmental drivers explain most of the diurnal variations in photosynthesis when leaf phenology barely changes within a day (*14*). Air temperature (T_{air}) and atmospheric dryness [or vapor pressure deficit (VPD)] are higher in the afternoon than in the morning (*15*, *16*), while the foliar water potential decreases

[1]Jiangsu Center for Collaborative Innovation in Geographical Information Resource Development and Application, International Institute for Earth System Sciences, Nanjing University, Nanjing, Jiangsu 210023, China. [2]Yuxiu Postdoctoral Institute, Nanjing University, Nanjing, Jiangsu 210023, China. [3]Jiangsu Provincial Key Laboratory of Geographic Information Science and Technology, Key Laboratory for Land Satellite Remote Sensing Applications of Ministry of Natural Resources, School of Geography and Ocean Science, Nanjing University, Nanjing, Jiangsu 210023, China. [4]European Commission, Joint Research Centre (JRC), Ispra, Italy. [5]CSIRO, Oceans and Atmosphere, Private Bag 1, Aspendale, Victoria 3195, Australia. [6]Department of Earth and Environmental Engineering, Columbia University, New York, NY, USA. [7]Earth Systems Research Center, Institute for the Study of Earth, Oceans, and Space, University of New Hampshire, Durham, NH, USA. [8]Research Institute of Water and Environmental Engineering (IIAMA), Department of Applied Physics, Polytechnic University of Valencia, Valencia, Spain. [9]School of Life Sciences, University of Technology Sydney, Sydney, New South Wales, Australia. [10]School of Biological Sciences, The University of Hong Kong, Pokfulam, Hong Kong. [11]State Key Laboratory of Agrobiotechnology, The Chinese University of Hong Kong, Shatin, Hong Kong, China. [12]Department of Geography and Planning, University of Toronto, Toronto, Ontario, Canada. [13]CSIC, Global ecology Unit CREAF-CSIC-UAB, Bellaterra 08193, Catalonia, Spain. [14]CREAF, Cerdanyola del Vallès 08193, Catalonia, Spain. [15]International Joint Carbon Neutrality Laboratory, Nanjing University, Nanjing, Jiangsu 210023 China.
*Corresponding author. Email: yongguang_zhang@nju.edu.cn

from morning to afternoon due to the loss of water through transpiration and then recovers overnight (*17*–*19*). These processes can induce different responses of photosynthesis and ET to T_{air} and VPD between morning and afternoon. The difference in the fluxes of carbon and water between morning and afternoon provides key information on the physiological responses of plants to environmental drivers and potential constraints on primary productivity (*15*). For example, an afternoon depression of photosynthesis is a typical indicator of stomatal stress due to high VPD, whereas a symmetric pattern between morning and afternoon suggests that photosynthesis is predominantly light limited (*15*).

Diurnal variations in photosynthesis and ET have been measured at a few eddy covariance (EC) flux sites across the Amazon forest, where afternoon reductions in photosynthesis and ET have been observed (*16*). However, these flux sites are sparsely distributed across the region and may not fully represent the complex geographical patterns in vegetation and climate of the Amazon forest (*20*), resulting in a clear gap in scaling up from site observations to regional estimates of photosynthesis and ET. At present, large-scale observations of diurnal variations in photosynthesis or ET of Amazon forests are lacking, limiting our understanding of the physiological regulation of carbon-water fluxes and their feedbacks to the climate.

The International Space Station (ISS) hosts a series of instruments that observe the Earth at different times throughout the day (*21*). Among these instruments, the Ecosystem Spaceborne Thermal Radiometer Experiment (ECOSTRESS) has been retrieving ET measurements since 2018 (*22*), and the Orbiting Carbon Observatory-3 (OCO-3) has been measuring solar-induced chlorophyll fluorescence (SIF) since 2019 (*23*). SIF is electromagnetic radiation emitted by leaf chlorophyll during the light reaction of photosynthesis (*24*) and can be retrieved from high spectral resolution atmospheric and meteorological space missions (*25*, *26*). Over the past decade, SIF has been shown to be a promising indicator of terrestrial photosynthesis (*25*, *27*, *28*) and for studying the seasonality of Amazonian forests (*29*, *30*) and their responses to drought (*31*, *32*) and aridity (*33*). However, because traditional sun-synchronous satellites pass over a given location on Earth at the same time each day, they cannot provide observations for different times of day over the Amazon.

Hence, the combination of ECOSTRESS ET and OCO-3 SIF provides a unique opportunity for studying the large-scale fluxes of carbon and water at the diurnal time scale. The diurnal photosynthesis and ET at regional scales are informative as how land-atmosphere interactions are regulated by changes in physiological responses to varying environmental conditions (*34*). In addition, the high T_{air} and VPD in the afternoon can mimic future conditions compared with current status. Thus, an analysis of the diurnal patterns of photosynthesis and ET from morning to afternoon can offer a unique view of their future trends and responses to climate change. Therefore, we aim to investigate the large-scale diurnal patterns of photosynthesis and ET in the Amazon forest and their responses to atmospheric warming and drying by combining ECOSTRESS ET with OCO-3 SIF.

Building on these ata streams, we investigated the large-scale diurnal patterns of photosynthesis and ET in the Amazon forest and SIF-based water use efficiency (WUE_{SIF} = SIF/ET) (*34*), which is a crucial indicator of the water use strategy in photosynthesis (*35*). We also analyzed the sensitivities of SIF, ET, and WUE_{SIF} to perturbations in environmental drivers [T_{air}, VPD, and soil moisture (SM)] and their differences between morning and afternoon. We further generated temporally and spatially continuous hourly total canopy SIF emission (denoted as SIF from here onward) and ET during 2015–2021 using random forest (RF) models trained with the response variables of OCO-3 SIF and ECOSTRESS ET and with the drivers of T_{air}, VPD, SM, radiation, and fraction of photosynthetic active radiation (FPAR) (see Materials and Methods). Using the RF models, we also projected changes in future photosynthesis and ET from 2015 to 2100 under a scenario of climate warming and increasing VPD based on the sixth phase of the Coupled Model Intercomparison Project (CMIP6). The limited biases related to the spatial extrapolations, temporal extrapolations, and future extrapolations does not affect our results and conclusions using RF models (see Material and Methods).

RESULTS

Diurnal patterns of photosynthesis and ET in Amazon forests

First, we explored the diurnal patterns of clear-sky SIF, ET, and WUE_{SIF} across the Amazon forest (fig. S1) based on the RF modeling from 2015 to 2021 (Fig. 1). Both carbon and water fluxes typically peaked around noon (11:00 to 13:00) (Fig. 2, A and D), and their diurnal variations were driven mainly by solar radiation and air temperature. SIF slightly increased from 7.69 $mW \cdot m^{-}2 \cdot nm^{-}1$ in the morning to 7.70 $mW \cdot m^{-}2 \cdot nm^{-}1$ in the afternoon in the wet season but decreased from 8.12 to 7.76 $mW \cdot m^{-2} \cdot nm^{-1}$ in the dry season (Fig. 2A), which was consistent with CMIP6 earth system model (ESM) simulations: slightly increasing in the morning and decreasing in the afternoon (Fig. 2C). Site-based gross primary production (GPP) also showed a larger afternoon decrease in the dry season than in the wet season (Fig. 2B), which can be attributed to the much higher VPD and T_{air} in the dry season afternoon (fig. S2). Such a higher water stress condition of the dry season afternoon is further observed to accompany with a reduction in ET by RF models (Fig. 2D) and a weak ET increase by site level flux observations (Fig. 2E), both of which are in large contrast to the substantial afternoon increase in wet season ET. CMIP6 ESMs simulated a similar afternoon increase in ET between the wet and dry seasons (Fig. 2F), showing that ESMs could not fully capture the effects of water stress on ET. In addition, the morning WUE_{SIF} was always higher than the afternoon WUE_{SIF}, consistent with WUE_{GPP} from both site-based flux observations and CMIP6 ESM simulations (Fig. 2, G to I). Because we simulated clear-sky SIF and ET using the symmetrical radiation around local solar noon, the differences in SIF and ET between morning and afternoon were not due to light effects but rather to increased T_{air} and VPD and the related stomatal regulation on photosynthesis and transpiration.

Next, we investigated the diurnal and seasonal patterns of carbon and water fluxes across the Amazon forest and the hysteretic responses of WUE to VPD, which have not yet been observed at the regional scale before. The amplitudes of the diurnal variations in both SIF and ET were greater than their respective seasonal variations (Fig. 3, A and B and fig. S3), and the relationships between SIF and ET differed significantly ($P < 0.001$, using one-way analysis of covariance) between the morning and afternoon in both the wet and dry seasons (Fig. 3, C and D). The results of the linear regression modeling showed that SIF was lower in the late afternoon than

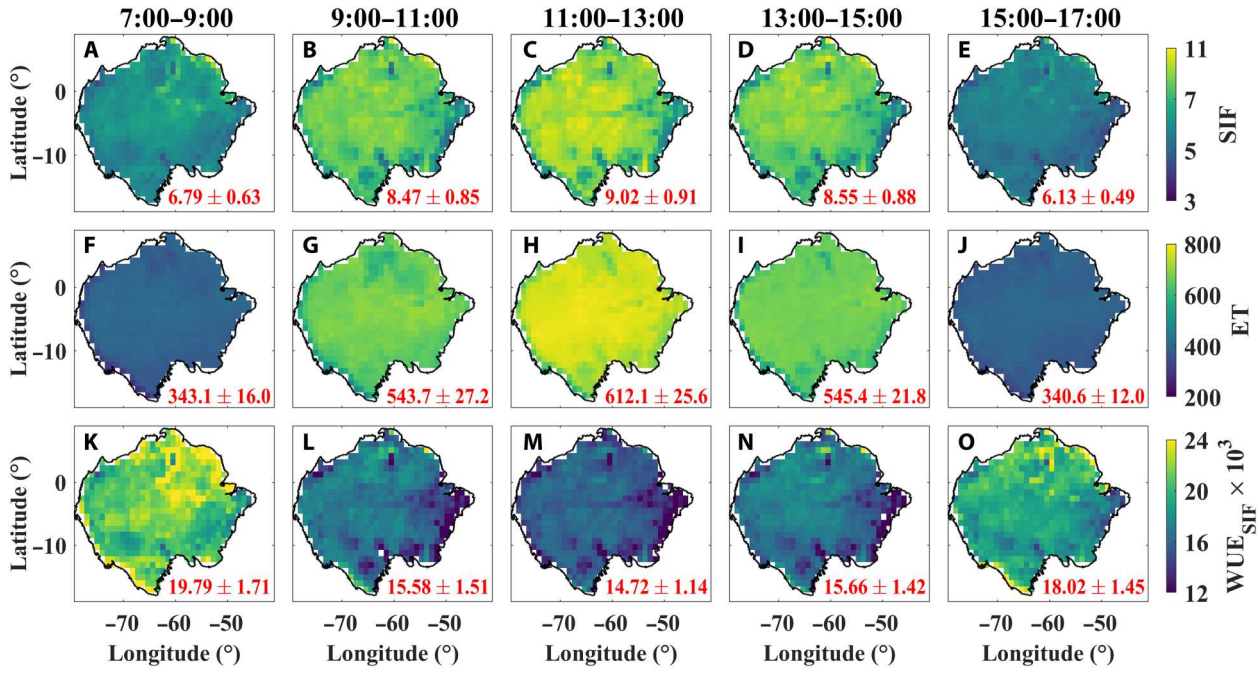

Fig. 1. Diurnal patterns of SIF (mW · m^{-2} · nm^{-1}), ET (W · m^{-2}), and WUE$_{SIF}$ (mW · m^{-2} · nm^{-1}/W · m^{-2}) in Amazonian forests throughout 2015–2020. W · m^{-2} Diurnal (**A** to **E**) SIF, (**F** to **J**) ET, and (**K** to **O**) WUE$_{SIF}$ (=SIF/ET) at 2-hour intervals: 7:00 to 9:00, 9:00 to 11:00, 11:00 to 13:00, 13:00 to 15:00, and 15:00 to 17:00. The mean and SD are shown in the bottom right of each panel. The spatial resolution is 1° × 1°.

in the early morning for the same level of ET, supporting the idea that WUE$_{SIF}$ declined during the day as VPD increased (Fig. 3, E and F). Moreover, the regional diurnal WUE$_{SIF}$ exhibited an oblique U-shaped, hysteretic relationship with VPD (Fig. 3, G and H). The hysteresis of WUE$_{SIF}$-VPD suggests that the relationship between photosynthesis and ET as quantified by WUE$_{SIF}$ changes during the day, most likely because of a decline of water content in the plant system and an increased sensitivity of stomatal conductance to VPD in the afternoon.

To assess how the hysteresis of WUE$_{SIF}$-VPD varied spatially, we selected three subregions in eastern, northwestern, and southwestern Amazon (three boxes in fig. S4) that differ in canopy structure, phenology, and rainfall and found that the hysteretic responses of WUE$_{SIF}$ to VPD varied spatially across the three regions (Fig. 4), indicating that the limited site observation cannot adequately represent all the forests in the Amazon region. The strongest hysteretic response of WUE$_{SIF}$ to VPD was observed in drier regions, such as the eastern Amazon in the dry season (Fig. 4E). The oblique U-shaped relationships between WUE$_{SIF}$ and VPD across different subregions were consistent with surface flux observations at three Amazonian sites (BR-Sa1, BR-Sa3, and GF-Guy) (figs. S5 to S7). These results indicated that our regional hourly SIF and ET captured well the diurnal, spatial, and seasonal variations in photosynthesis and ET and their responses to environmental drivers.

To quantify the Amazonian diurnal variations in the ecosystem fluxes of carbon and water, we compared SIF, ET, and WUE$_{SIF}$ between morning (7:00 to 12:00) and afternoon (12:00 to 17:00). Clear spatial variations were observed for SIF, ET, and WUE$_{SIF}$ in both the wet and dry seasons (fig. S8). For example, WUE$_{SIF}$ during the dry season was generally lowest in the east with relatively younger forest (fig. S9), where VPD was high and SM was low (fig. S2). Marginal diurnal changes in SIF were observed during the wet season (Fig. 5A), indicating that photosynthesis was mostly light limited when T_{air} and VPD were low (fig. S2, A and F) and SM was high (fig. S2K). However, during the dry season, SIF decreased from morning to afternoon (Fig. 5B), especially in the southeastern part of the Amazon where rainfall was low and T_{air} and VPD were high. ET increased and decreased diurnally over much of the Amazon in the wet and dry seasons, respectively (Fig. 5, C and D), with a shift from a demand-limited regime to a supply-limited regime. Therefore, these results revealed varying effects of T_{air} and VPD on photosynthesis and ET between the wet and dry seasons.

Sensitivities of photosynthesis and ET to environmental drivers

The afternoon depressions of photosynthesis and ET in the dry season (Fig. 5, B and D) provide unique insights on how land-atmosphere interactions will respond to future climatic warming and atmospheric drying, but it is unclear how individual environmental drivers (such as T_{air}, VPD, and SM) affect the fluxes of carbon and water at the diurnal scale. Particularly, the effects of T_{air}, VPD and incoming solar radiation were commonly mixed due to their high correlations (fig. S10). To distinguish between the interdependent effects of environmental drivers on the fluxes of carbon and water, we analyzed the sensitivities of SIF, ET, and WUE$_{SIF}$ using RF models (see Materials and Methods).

The results showed positive sensitivity of SIF to VPD (in other words, SIF would increase with VPD) in the morning more than 98.7% and 70.9% of the region in the wet and dry seasons, respectively (Fig. 6, A, B, and D), after factoring out the effects of other drivers. The negative sensitivity of photosynthesis to VPD in the

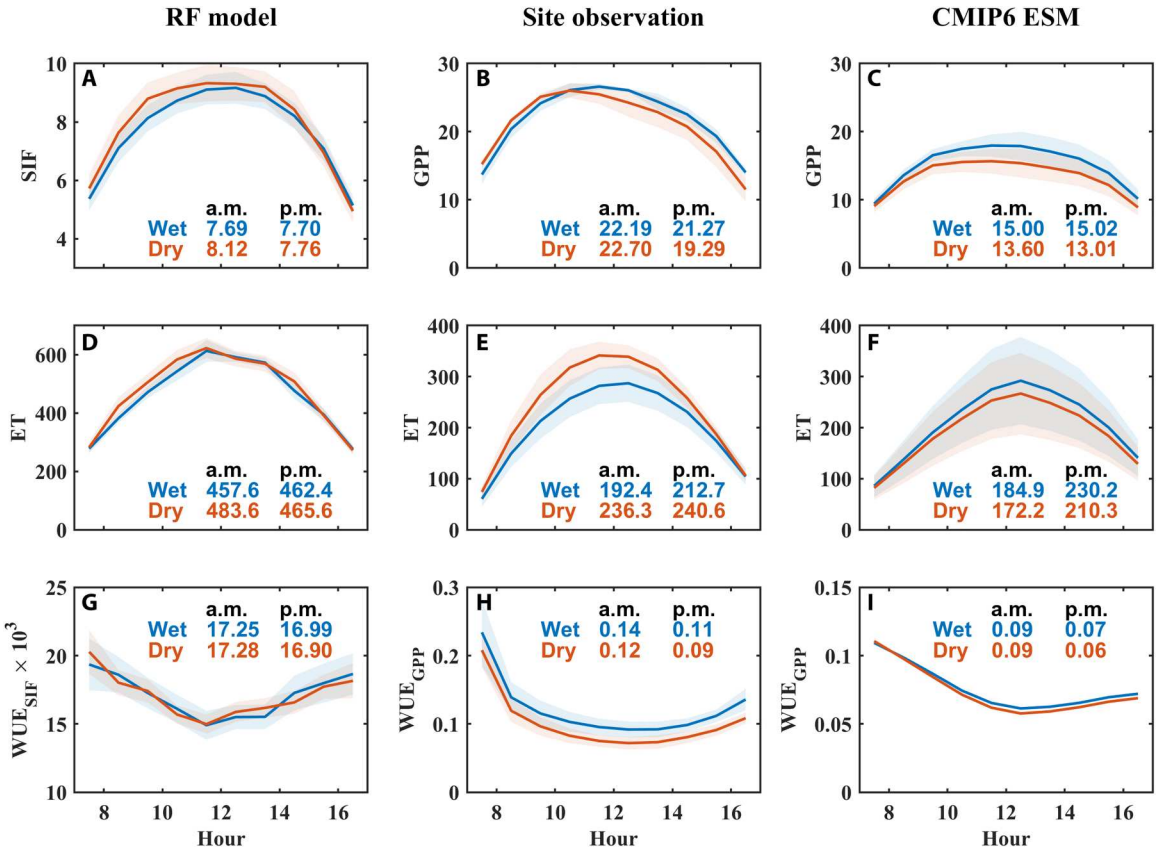

Fig. 2. Diurnal patterns of energy, carbon, and water fluxes in Amazonian forests for wet and dry seasons. The RF models generated (**A**) SIF ($mW \cdot m^{-2} \cdot nm^{-1}$), (**D**) ET ($W \cdot m^{-2}$), and (**G**) WUE_{SIF} ($mW \cdot m^{-2} \cdot nm^{-1}/W \cdot m^{-2}$) averaged over 2015–2021. The shaded area represented the one SD across the Amazon forest. Site-based eddy flux-derived (**B**) GPP ($\mu mol \cdot m^{-2} \cdot s^{-1}$), (**E**) ET ($W \cdot m^{-2}$), and (**H**) WUE_{GPP} ($\mu mol \cdot m^{-2} \cdot s^{-1}/W \cdot m^{-2}$). The shaded area represented the one SD across three sites (BR-Sa1, BR-Sa3, and GF-Guy). CMIP6 ESM simulated historical (**C**) GPP ($\mu mol \cdot m^{-2} \cdot s^{-1}$), (**F**) ET ($W \cdot m^{-2}$), and (**I**) WUE_{GPP} ($\mu mol \cdot m^{-2} \cdot s^{-1}/W \cdot m^{-2}$) averaged over 2000–2014. The shaded area represented the one SD across ESMs. More details about the sites and CMIP6 ESM can be found in tables S1 and S2, respectively. The averages of morning (a.m.) and afternoon (p.m.) were shown in blue and orange for the wet and dry seasons, respectively.

dry season morning mainly occurred in the nonforest regions (such as grass and savanna). The sensitivity of SIF to VPD also showed a clear northwest-southeast gradient from being positive to being negative in the dry season morning, indicating that the super-wet northwest Amazon was not VPD stressed. However, the afternoon SIF exhibited negative sensitivity to VPD more than 74.5 and 67.4% of the region in the wet and dry seasons, respectively (Fig. 6, A, C, and E). Moreover, asymmetric responses of SIF to T_{air} between morning and afternoon were observed in the dry season (Fig. 7, A, D, and E). Different from SIF, ET showed consistently negative sensitivities to VPD (Fig. 6, F to J) in the morning or afternoon in both dry and wet seasons but positive sensitivities to T_{air} (Fig. 7, F to J). These results stressed the importance of stomatal control on the ET of the Amazon that is able to reverse the sensitivity of ET to VPD (i.e., plants are transpiring less when the atmospheric demand is higher). Consequently, WUE_{SIF} was positively sensitive to VPD (Fig. 6, K to O) but negatively sensitive to T_{air} (Fig. 7, K to O); therefore, forests varied their water use strategies under different temperature and atmospheric dryness stresses. Given the small variations in SM during the course of the day, SIF and ET exhibited weaker sensitivities to SM (fig. S11) than to VPD and T_{air}. The combined negative sensitivities of SIF to T_{air} and VPD in the dry season afternoon led to a decrease in SIF, which is a sign of what could happen in Amazonian forests under the projected atmospheric warming and drying in the future.

Next, we quantified the large-scale afternoon depressions of SIF, ET, and WUE_{SIF} following increases in T_{air} and VPD. For this purpose, we applied the afternoon RF model to the morning conditions during 2015–2021 (see Materials and Methods). The results of this process were considered in the "$model_{PM}$ + $condition_{AM}$" simulations and were compared with the "$model_{AM}$ + $condition_{AM}$" simulations. SIF and ET decreased by 4.4 ± 1.5 and 2.1 ± 2.8%, respectively, from the $model_{AM}$ + $condition_{AM}$ simulations to the $model_{PM}$ + $condition_{AM}$ simulations in the wet season (Fig. 8, A and C); these decreases were stronger in the dry season (Fig. 8, B and D). The stronger reduction in SIF than ET led to decreases in WUE_{SIF} by 2.2 ± 3.6 and 0.6 ± 3.5% in the wet and dry seasons, respectively (Fig. 8, E and F). Therefore, the strong afternoon reductions in SIF and ET point to the stronger asymmetric responses of photosynthesis and ET to atmospheric warming and drying in the dry season than in the wet season in the Amazon forest.

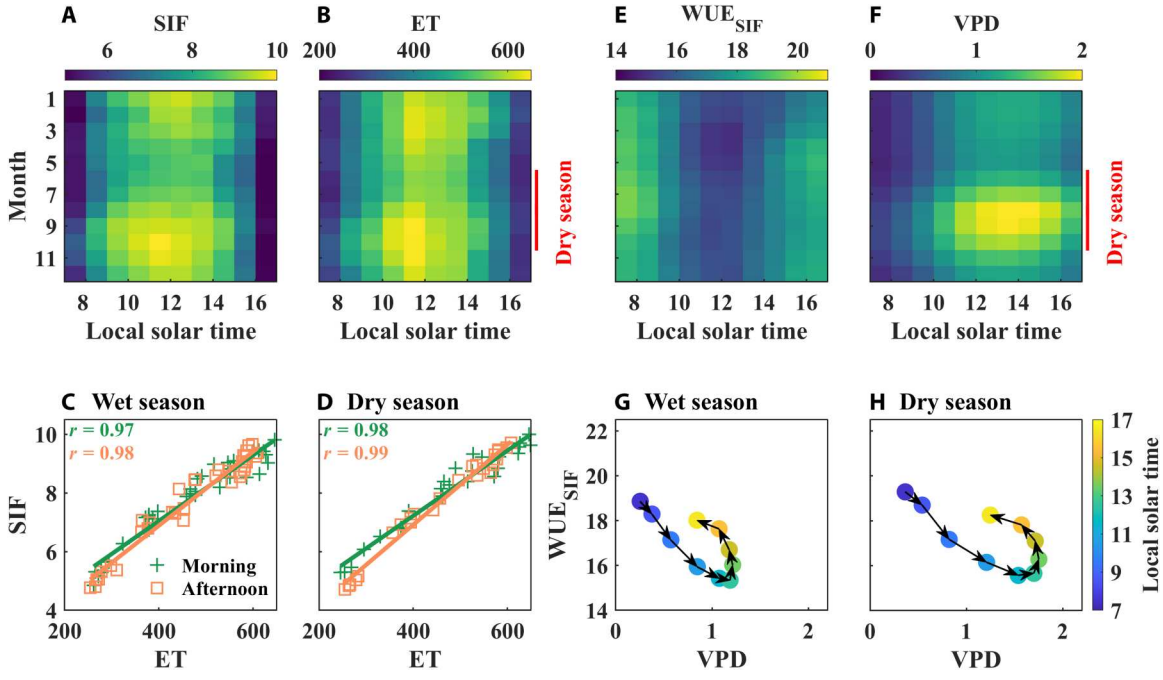

Fig. 3. Seasonal and diurnal patterns (shown as fingerprints) of SIF (mW · m^{-2} · nm^{-1}), ET (W · m^{-2}), WUE$_{SIF}$ (mW · m^{-2} · nm^{-1}/W · m^{-2}), and VPD (kPa) throughout the Amazon forest. (**A**) SIF, (**B**) ET, (**E**) WUE$_{SIF}$, and (**F**) VPD. The red vertical lines represent the dry season from June to October. The SIF and ET were derived on the basis of the RF models during 2015 and 2021, and VPD was from the ERA5 reanalysis data during 2015 and 2021. The linear relationships between SIF and ET in the (**C**) wet and (**D**) dry seasons, with crosses (morning) and squares (afternoon) representing average hourly values at a monthly temporal resolution in (A) and (B). The relationships between hourly WUE$_{SIF}$ and VPD averaged over the (**G**) wet and (**H**) dry seasons. The black arrows represent the directions of variations in diurnal WUE$_{SIF}$ and VPD.

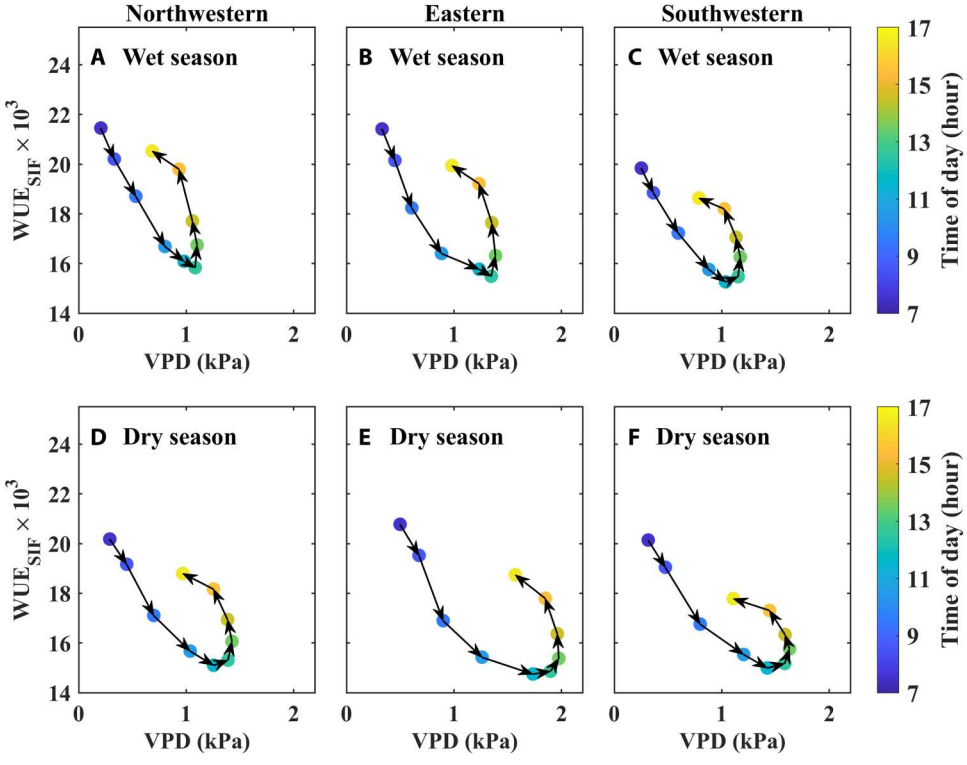

Fig. 4. Relationships between WUE$_{SIF}$ and VPD for the different regions. (**A** to **C**) Northwestern, eastern, and southwestern Amazon Basin (red, blue, and black boxes, respectively, in fig. S4). The dots represent the seasonal averages, with the colors indicating the time of day. (**D** to **F**) similar to (A) to (C) but for the dry season.

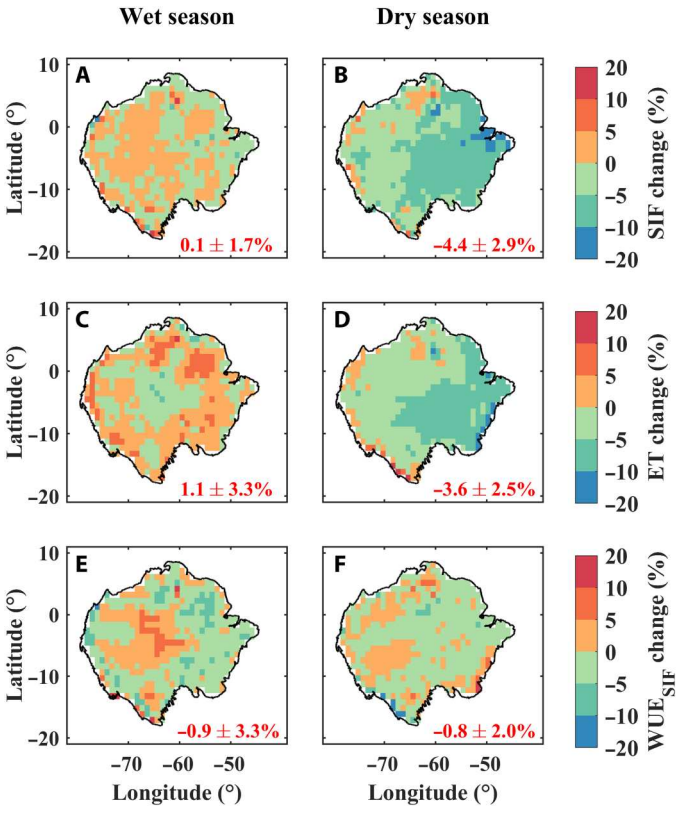

Fig. 5. Difference in SIF, ET, and WUE_{SIF} between morning (7:00 to 12:00) and afternoon (12:00 to 17:00) in Amazonian forests. (**A** and **B**) Spatial distributions of percentage changes in SIF from morning to afternoon in the wet and dry seasons, respectively. The mean and SD are shown in the bottom right of each panel. (**C** to **F**) are similar to (A) and (B) but for ET and WUE_{SIF}, respectively.

Projections of photosynthesis and ET under atmospheric warming and drying

The RF models were used to predict future changes in Amazonian morning and afternoon photosynthesis and ET from 2015 to 2100 using the CMIP6 model simulations as inputs for the shared socioeconomic pathways (SSPs) SSP245, SSP370, and SSP585 (*36*). We did not consider the CO_2 fertilization effect and changes in forest composition or structure. The morning SIF in the wet season increased by 4, 6, and 8% from 2015 to 2100 under SSP245, SSP370, and SSP585, respectively (Fig. 9A), but the increases in the afternoon SIF were weaker (Fig. 9B). Accordingly, the daily SIF in the wet season increased (Fig. 9C), which was consistent with the CMIP6 model simulations of GPP, although there was a difference in magnitude between our results and CMIP6 simulations (Fig. 9D). The changes from 2015 to 2100 in ET in the wet season were much smaller than those in SIF or GPP (Fig. 9, E to H). In the dry season, an increase in the morning SIF (Fig. 9I) was offset by the decrease in the afternoon SIF (Fig. 9J). Consequently, only marginal changes in the daily SIF in the dry season were projected (Fig. 9K). However, CMIP6 models predicted increasing trends of primary productivity under future climate warming in the Amazon (Fig. 9L), which could be dominantly driven by the CO_2 fertilization effects. The morning ET in the dry season increased by 3, 4, and 5% from 2015 to 2100 under SSP245, SSP370, and SSP585, respectively, but the afternoon ET was nearly constant. As a result, daily ET increased (Fig. 9, M and N). The widespread reductions in SIF (89%) and ET (77%) in the dry season afternoon were predicted by the end of this century under SSP585 (figs. S12 and S13). On the basis of our data stream of diurnal SIF and ET, our results revealed stronger sensitivity to atmospheric dryness leading to overall a neutral response of Amazonian photosynthesis to atmospheric warming and drying in the future dry season.

DISCUSSION

Differences in diurnal patterns of photosynthesis and ET between wet and dry seasons

This study uses a combination of satellite-based data from two instruments (ECOSTRESS and OCO-3) aboard the ISS to study the large-scale diurnal patterns of photosynthesis and ET over the Amazon forest and their responses to environmental drivers. We reveal different large-scale diurnal patterns of photosynthesis and ET between wet and dry seasons in the Amazon forest (Fig. 3), which have not been observed at regional scale. The photosynthesis and ET across the Amazon forest did not decrease from morning to afternoon in the unstressed wet season but decreased in the dry season (Fig. 2, A and D), which could be attributed to the decreases in mesophyll (*37*) and stomatal conductance (*15*) in response to high VPD (fig. S2J) and decreased leaf water potential during the day. The stronger stresses on photosynthesis and ET in the dry season than in the wet season were also supported by site-based flux observations: Photosynthesis decreased more, and ET increased less from morning to afternoon in the dry season than in the wet season (Fig. 2, B and E).

The different diurnal patterns of ET between wet and dry seasons could be partly attributed to the strong interplay between SM and VPD on leaf water potential and therefore on stomatal behavior (*15*). Because the decrease in SM from morning to afternoon was very small, SM had a weak direct effect on ET at the diurnal scale. However, the difference in SM between wet and dry season regulates predawn leaf water potential (*38*). In the wet season (SM is high), the high predawn leaf water potential resulted in low stomatal sensitivity to VPD. In the dry season with low SM, leaf water potential could reach a critical threshold, inducing partial stomatal closure at high VPDs and hence the decrease in ET. A recent study also pointed out that plants could either positively or negatively regulate water use depending on the water potential of the leaves (*39*). In other words, ET increased when water stress was limited and ET was demand limited (e.g., in the wet season) following an increase in evaporative demand. In contrast, ET decreased due to stomatal closure in response to substantial water limitation, leading to a decrease in ET (e.g., in the dry season).

Asymmetric responses of photosynthesis to VPD and T_{air}

These results raise a question of whether the response of photosynthesis to VPD would be different between morning and afternoon in the humid topics; for example, photosynthesis could be positively and negatively sensitive to atmospheric dryness in the morning and afternoon, respectively (Fig. 6). The positive sensitivity of photosynthesis to VPD in wet environment could not be attributed to the correlation between VPD and radiation in the morning because radiation remained unchanged using the sensitivity analysis (see Materials and Methods). Rainfall interception by leaves and

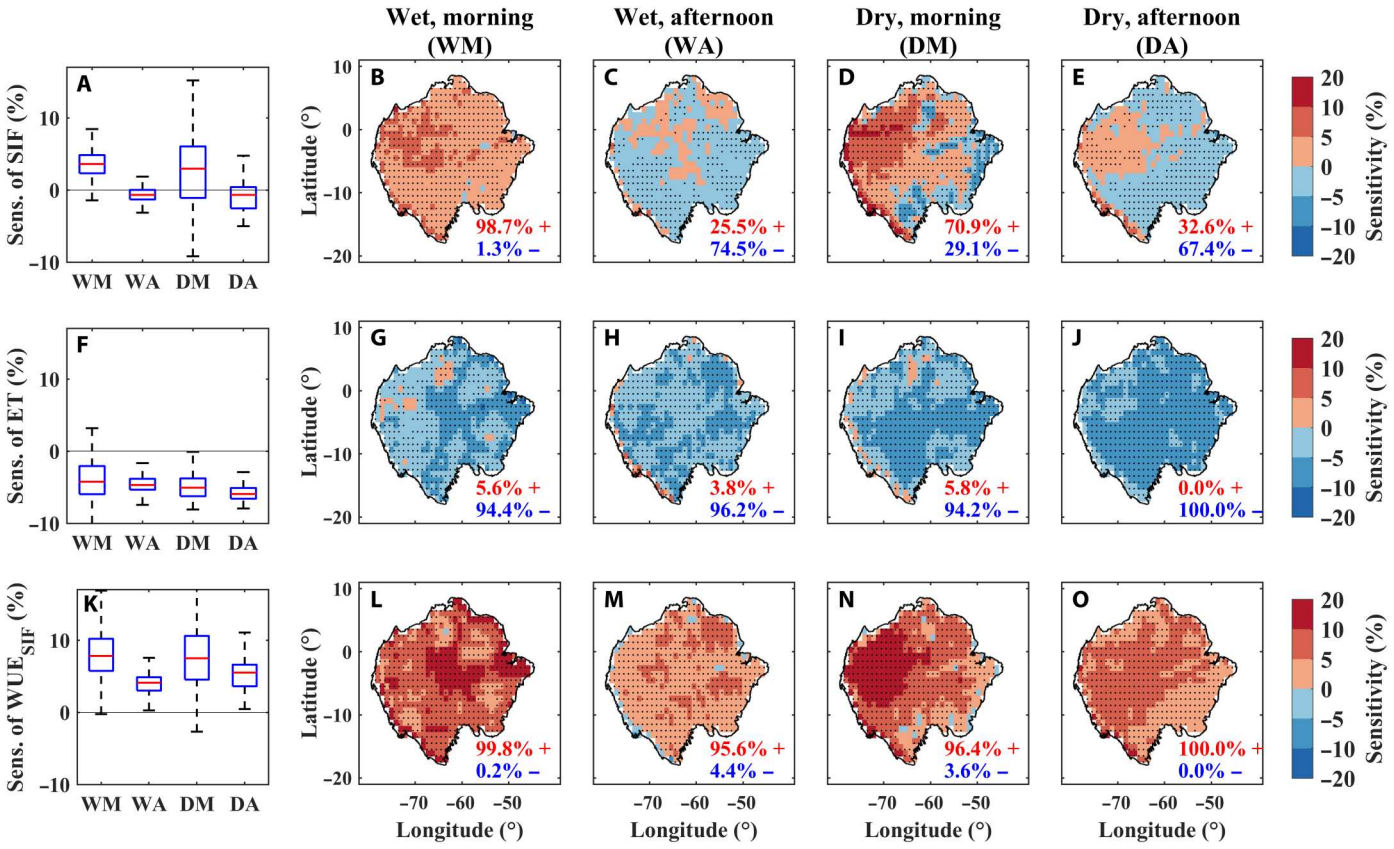

Fig. 6. RF-based sensitivity analysis of SIF, ET, and WUE$_{SIF}$ to VPD. (**A**) Box plots of the sensitivity of SIF to an increase in VPD by one SD for the wet season morning (WM), wet season afternoon (WA), dry season morning (DM), and dry season afternoon (DA, the period when foliar and soil water potentials are lowest and stress is highest). (**B** to **E**) The spatial distribution of the sensitivity of SIF to VPD. (**F** to **J**) and (**K** to **O**) are similar to (A) to (E) but display the sensitivities of ET and WUE$_{SIF}$ to VPD, respectively. These sensitivities were derived as partial dependences, assuming that other drivers did not vary with VPD. The red line in each box plot indicates the median, and the bottom and top edges of the box indicate the 25th and 75th percentiles, respectively. The stippling on the maps represents regions where at least 95% of the RF models agree on the sign of the sensitivity. The numbers in the bottom right corner of each map panel are the area percentages of positive (+, red) and negative (–, blue) sensitivities.

morning dew can limit photosynthesis by reducing light availability and slowing carbon diffusion (*40*). Drier air can facilitate the rate of evaporation from wet foliar surfaces, thus reducing morning fog and increasing light absorption earlier in the day (*41*) and hence photosynthesis and SIF. The positive sensitivity of morning SIF to VPD in this work is consistent with a recent study reporting that SIF derived from Global Ozone Monitoring Experiment–2 (~9:30 overpass time) was positively sensitive to VPD in the Amazon rainforest (*33*). However, we further found that the positive effect of VPD on photosynthesis mostly disappeared in the afternoon, by then the dew would already have evaporated. In addition, we also found the asymmetric responses of SIF to T_{air} in the dry season but not in the wet season. This could depend on whether T_{air} reached the optimum temperature for photosynthesis (T_{opt}, estimated at around 30°C for tropical forests) (*42*), indicating that T_{air} exceeded T_{opt} in the dry season afternoon and hence photosynthesis reduced.

The asymmetric responses of photosynthesis to VPD and T_{air} between morning and afternoon in the humid tropics were not observed at regional scale based on SIF from sun-synchronous satellites that passed over at a fixed time, thus highlighting the importance of OCO-3 SIF and ECOSTRESS ET observations for studying the physiological responses of Amazonian forests to atmospheric warming and drying and their compound effects with soil drying, offering a window onto future physiological changes in the Amazon. Although these results indicate that SIF from existing sun-synchronous satellites cannot fully reveal the physiological responses to varying environmental drivers at the diurnal scale, it is still feasible to use SIF based on sun-synchronous satellites to study the seasonality of photosynthesis and phenology (*29*, *30*, *43*) because the diurnal bias does not affect the overall seasonality of photosynthesis.

Different water use strategies under temperature and atmospheric dryness stresses

On the basis of the sensitivity analysis, this study identified the different large-scale water-use strategies of Amazonian forests under temperature and atmospheric dryness stresses: WUE$_{SIF}$ increased with VPD (being conservative; Fig. 6, K to O) and decreased with T_{air} (Fig. 7, K to O). Therefore, ET decreased to reduce water losses to reduce the risk of hydraulic failure under high VPD (*44*), leading to increasing WUE$_{SIF}$. However, under high temperature and ample water supply, humid tropical forests reduced their WUE$_{SIF}$ (less conservative) by increasing ET to lower foliar temperature (for cooling) for maintaining high photosynthetic rates (*45*). The

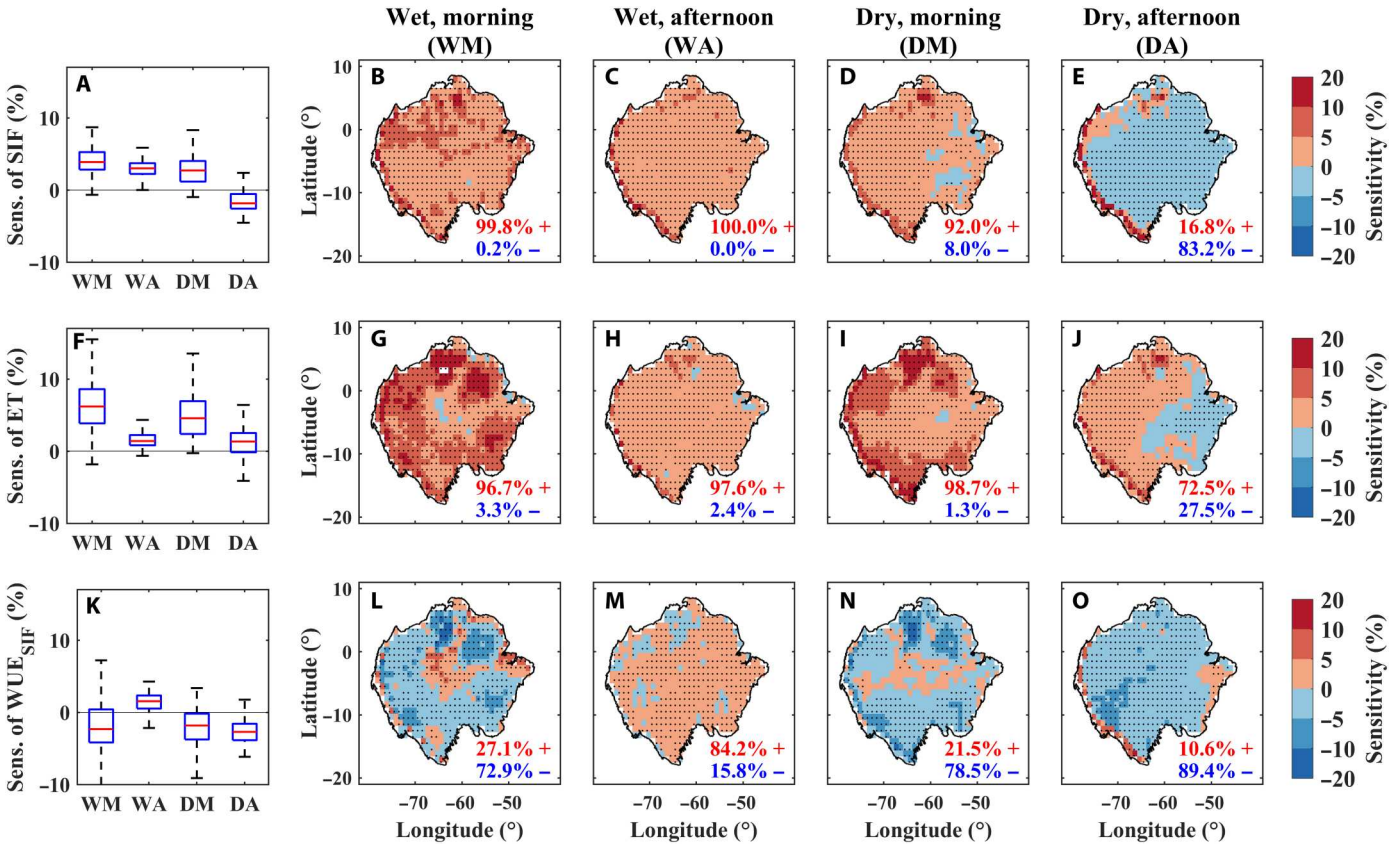

Fig. 7. RF-based sensitivity analysis of SIF, ET, and WUE_{SIF} to . T_{air} (**A**) Box plots of the sensitivity of SIF to an increase in T_{air} by one SD for the wet season morning (WM), wet season afternoon (WA), dry season morning (DM) and dry season afternoon (DA, the period when foliar and soil water potentials are lowest and stress is highest). (**B** to **E**) Spatial distribution of the sensitivity of SIF to T_{air}. (**F** to **J**) and (**K** to **O**) are similar to (A) to (E) but display the sensitivities of ET and WUE_{SIF} to T_{air}, respectively. These sensitivities were derived as partial dependences, assuming that other drivers did not vary with T_{air}. The red line in each box plot indicates the median, and the bottom and top edges of the box indicate the 25th and 75th percentiles, respectively. The stippling on the maps represents regions where at least 95% of the RF models agree on the sign of the sensitivity. The numbers in the bottom right corner of each map panel are the area percentages of positive (+, red) and negative (–, blue) sensitivities.

decreases in WUE_{SIF} from morning to afternoon indicate a dominant role of the cooling mechanism in regulating WUE_{SIF} for humid tropical forests. The decrease in WUE_{SIF} is opposite to what would be predicted by the widely used model of stomatal conductance based on optimality principles (*46*), i.e., minimizing water losses while maximizing photosynthesis. Such an inconsistency with optimal stomatal models was also observed from a warming experiment (*47*). Our results suggest that stomatal models based on optimality principles may underestimate the role of ET as a key cooling mechanism in the humid tropical forests in response to temperature stress.

Neutral changes of Amazon photosynthesis and ET in the dry season

We projected that both diurnal (morning and afternoon) and seasonal (wet and dry) variations of photosynthesis and ET in the Amazon forest will change under future atmospheric warming and drying conditions (Fig. 9). Assuming a similar species composition and no major CO_2 fertilization effect, photosynthesis will likely increase in the unstressed wet season and in the mornings of the dry season in the humid tropics, supporting the positive effect of warming on photosynthesis under adequate soil water supply (*48*). However, this positive effect will not occur in the dry season afternoon due to increasing temperature (beyond T_{opt}) and atmospheric dryness, which will reduce the photosynthetic capacity and stomatal conductance (*3*, *44*). Therefore, we predict large-scale afternoon depressions of photosynthesis in the dry season. These diurnal variations do not contradict the dry season increase of photosynthesis and ET (*12*) because the seasonality of Amazon ecosystems is largely controlled by phenology (i.e., leaf quality and demography) (*14*), although the global seasonal and interannual variations in photosynthesis are also related to radiation (*49*) and water availability (*50*). Our results highlight the importance of incorporating more accurate representation of physiological responses driving carbon and water fluxes in "next-generation" Earth system models.

Diurnal CO_2 data have not been available at the regional scale, and therefore, atmospheric CO_2 concentrations were not included as a driver in our RF model, and the potential impact of increasing atmospheric CO_2 concentration on our simulations was therefore not considered. Because we mainly investigated the diurnal patterns of photosynthesis and ET and their responses to environmental drivers, ignoring CO_2 effects has little effect on the diurnal patterns. Therefore, the projections still present valuable information on the

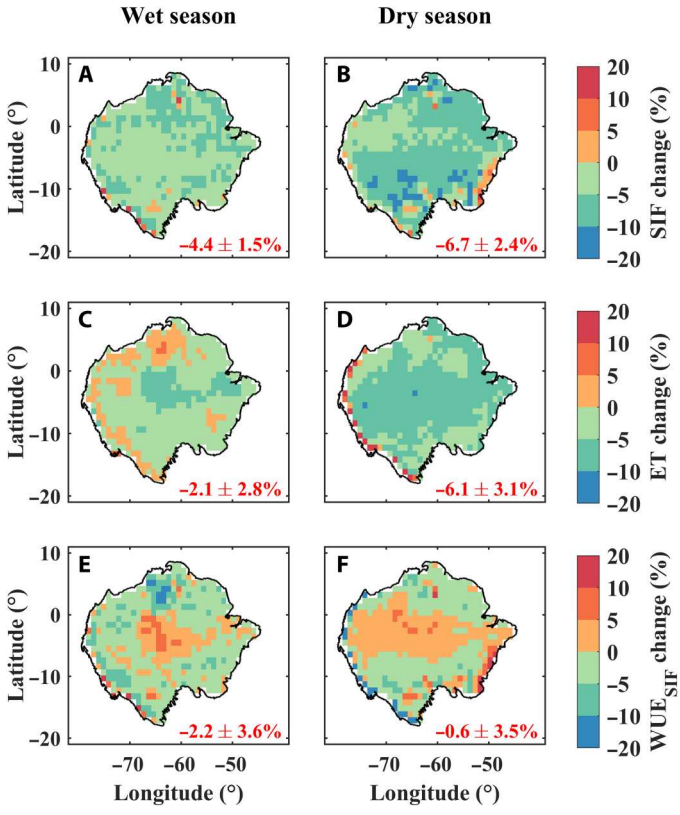

Fig. 8. Simulated percentage changes in SIF, ET, and WUE_{SIF} from the $model_{AM}$+ $condition_{AM}$ simulation to the $model_{PM}$+ $condition_{AM}$ simulation due to the increase in and VPD and decline in leaf water potential. T_{air} The $model_{AM}$ + $condition_{AM}$ and $model_{PM}$ + $condition_{AM}$ simulations were obtained by driving the morning and afternoon RF models using the morning inputs (including radiation, FPAR, VPD, T_{air}, and SM), respectively. (**A** and **B**) Percentage change in SIF from the $model_{AM}$ + $condition_{AM}$ to $model_{PM}$ + $condition_{AM}$ simulations in the wet and dry seasons, respectively. (**C** to **F**) are similar to (A) and (B) but for ET and WUE_{SIF}, respectively. The mean and SD are shown in the bottom right of each panel.

large-scale diurnal patterns of photosynthesis and ET. For example, the future increases in photosynthesis in the wet season are higher in the morning than in the afternoon. Even if considering the CO_2 fertilization effects, our projection still holds because of the strong and negative influences from the high afternoon T_{air} and VPD. As for the dry season, it is unclear whether the CO_2 fertilization effect could mitigate afternoon decreases of photosynthesis. This issue is beyond the scope of this study and deserves future study. CMIP6 ESMs include additional processes (such as CO_2 fertilization effects and atmospheric feedbacks), and they predict increasing GPP in both the wet and dry seasons. Given the notable atmospheric drying in the future dry season, the simulated similar increase in the dry season photosynthesis (Fig. 9L) as the wet season photosynthesis (Fig. 9D) by the CMIP6 ESMs suggests that ESMs did not fully accurately represent the negative VPD effects on photosynthesis, and likely overestimate photosynthesis and potentially also the terrestrial sink strength of the Amazon forest under future climatic conditions.

In summary, we used a combination of satellite observations to assess the large-scale diurnal patterns of photosynthesis and ET and their drivers over the entire Amazon forest. We identified reductions in regional photosynthesis and ET from morning to afternoon in the dry season and quantified this effect at an unprecedented spatial scale through an observation-driven analysis. Our large-scale diurnal patterns of photosynthesis and ET provided a strong observational basis for modeling the exchanges of carbon and water fluxes between the land and atmosphere in the Amazon forest. This study would also improve our understanding of the direction and magnitude of ecosystem fluxes in response to climate change in other tropical forests. We envisage that these findings will pave the way for the use of high-frequency observations made by satellite-based sensors in studies of plant functioning and ecosystem processes to better project future changes in the terrestrial carbon and water cycles.

MATERIALS AND METHODS

OCO-3 SIF

SIF is tightly linked to photosynthesis and is a good proxy of GPP at the ecosystem scale (*25*, *27*, *28*). The varying overpass time of the ISS allowed us to derive the diurnal pattern of SIF over the Amazon forest from OCO-3 SIF data (v10) (*23*, *51*), which has been used in a recent perspective article (*34*). Figure S1B shows the footprints of OCO-3 from January to February 2020 as an example, which present the variations in observation time (local solar time) for each path. We used OCO-3 SIF located in the Amazon forest from August 2019 to December 2021. OCO-3 provides SIF data at both 757 and 771 nm, but we used only the 757-nm SIF data due to their stronger signal (*52*). We also retained only the observations at nadir (viewing zenith angle near zero) and removed low-quality data, which were characterized as having a quality flag of >1.

We investigated the diurnal patterns of SIF over the Amazon forest using observations from OCO-3 on the ISS. However, the sun-target-viewing geometry effects on satellite SIF observations are particularly relevant for OCO-3, given the wide range of solar zenith angles (SZA) observed during the diurnal cycle. Therefore, we corrected the sun-target-viewing geometry effects in SIF data acquired by the OCO-3 sensor on the ISS (SIF_{obs}) by deriving the total canopy SIF emission (SIF_{total}) based on a reflectance-based method, which has been widely used in previous studies (*52*–*54*)

$$SIF_{total} = SIF_{obs}/f_{esc} \times \pi \quad (1)$$

$$f_{esc} = NIR_v/i_0 \times K \quad (2)$$

$$NIR_v = (NIR - R)/(NIR + R) \times NIR \quad (3)$$

$$i_0 = 1 - \exp(-G \times CI \times LAI/\cos SZA) \quad (4)$$

where f_{esc} is the probability of the escape of fluorescence from the canopy in the direction of observation, NIR_V is the near-infrared reflectance of vegetation, R and NIR are the reflectance at red and near-infrared bands, respectively, i_0 is canopy interception, ω is foliar leaf albedo at the band of 757 nm, G is the value of a G function, CI is clumping index, LAI is leaf area index, and cosSZA is the cosine of SZA. R and NIR were simulated with the RossThick-LiSparseR (RTLSR) Bidirectional Reflectance Distribution Function

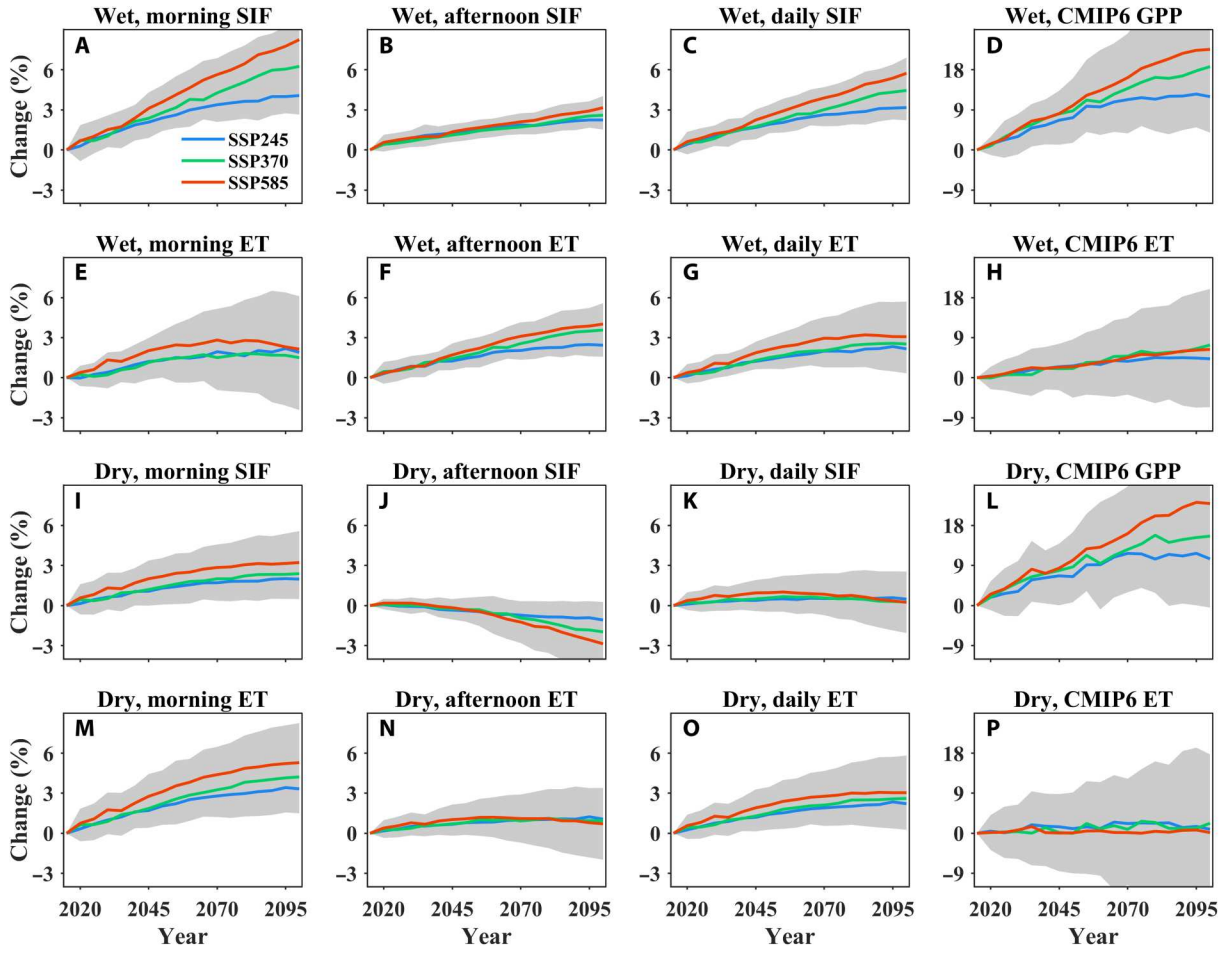

Fig. 9. Projections of relative changes in SIF and GPP from 2015 to 2100 across the Amazon forest. Projected changes in SIF in the wet season morning (**A**), wet season afternoon (**B**), wet season daily average (**C**), and CMIP6 daily average GPP in the wet season (**D**). The gray areas are the overlapped regions of one SD across different CMIP6 models for three SSP scenarios. To reduce the interannual variation, these data were smoothed using a 5-year running average. (**E** to **H**) similar to (A) to (D) but for ET. (**I** to **P**) similar to (A) to (H) but for the dry season.

model using the sun-target-viewing geometry of OCO-3 SIF. The parameters provided by the MCD19A3 BRDF/albedo product were used to drive the RTLSR model. For Amazonian forests, K was set at 1.2, G was set at 0.5, and CI was set at 0.66. LAI data were obtained from Copernicus LAI products (see below). SIF_{total} is referred to as SIF for simplicity elsewhere in the manuscript.

ECOSTRESS ET and T

The ECOSTRESS, a thermal radiometer built by the Jet Propulsion Laboratory of the National Aeronautics and Space Administration, is also aboard the ISS. ECOSTRESS measures thermal infrared radiation in five bands, which are used to generate higher level products, such as surface temperature and ET. ECOSTRESS and OCO-3 follow similar acquisition schedules at different times of day, which enabled us to explore the diurnal cycle of ET (fig. S1C). We used the ECOSTRESS ET product computed with the ET_PT–JPL algorithm (*55*). We used ECOSTRESS ET located in the Amazon forest from July 2018 to December 2021. Observations under cloudy conditions were excluded from the analysis based on the quality control flag. A preliminary validation study demonstrated that ECOSTRESS ET performed well against site measurements at 82 EC sites around the world (*22*). In addition to ET, ECOSTRESS level 3 products also provide the fraction of transpiration (T) in ET (T/ET), but the retrieval accuracy of T/ET has not been extensively assessed due to the lack of ground validation data. In addition, the T/ET provided by ECOSTRESS (fig. S14) was lower than previously reported values as it is less constrained by observations (*56*). Therefore, we did not use T.

Calculation of SIF-based WUE

The coupling of carbon and water was studied by developing a metric, SIF-based water-use efficiency (WUE_{SIF} = SIF_{total}/ET) (*34*), which is a proxy for GPP-based WUE (WUE_{GPP} = GPP/ET). ECOSTRESS' level 4 WUE was not used because it was calculated from ET and eight-day MODIS GPP. WUE_{GPP} is an indicator of the adjustment of photosynthesis to the loss of water, and has been studied many times at the seasonal and yearly scales globally (*35*). The magnitude of WUE often corresponds to the strategy of water use by plants, with higher WUEs indicating a more conservative strategy and lower WUEs indicating a less conservative strategy. The derived patterns of the relationship between VPD and WUE_{SIF} (Fig. 3, G and H) were consistent with those between VPD and

WUE_{GPP} based on the surface EC flux measurements (figs. S5 to S7), and uncorrected SIF_{obs}-based WUE (WUE_{SIFobs} = SIF_{obs}/ET) had reverse relationships with VPD (fig. S15), demonstrating the necessity of correcting the sun-target-viewing effects of SIF_{obs}.

Copernicus LAI

We used LAI data from the Copernicus Global Land Service LAI (version GEOV2). The Copernicus LAI dataset was derived using a near real-time algorithm based on an artificial neural network. Copernicus LAI was released at 10-day intervals and was linearly interpolated into a daily interval. Copernicus LAI was used to estimate i_0 in Eq. 4 above and then used to estimate diurnal FPAR (*57*)

$$\mathrm{FPAR} = (1 - 0.05) - (1 - 0.06) \times (1 - i_0) \quad (5)$$

ERA5 reanalysis

We acquired air temperature (T_{air}), dew-point temperature (T_{dew}), downward surface solar radiation (DSSR), and clear-sky DSSR from the fifth ECMWF ReAnalysis (ERA5) hourly data, which cover the global surface and have a spatial resolution of 0.25°. T_{air} and T_{dew} were used to calculate the VPD using the equation described in a previous study (*58*). To match satellite SIF and ET observations, linear interpolation was used to interpolate these meteorological data based on the latitude, longitude, and overpass time of the satellite observations. The DSSR and clear-sky DSSR, as proxies of PAR, were used to calculate the absorbed PAR (APAR). Because both the satellite SIF and ET data were filtered for cloudy conditions, they were better correlated with clear-sky APAR than with all-sky APAR (fig. S16), and hence clear-sky DSSR was used.

Eddy flux data

To compare with results from satellite observations, we used EC measurements from three flux sites (BR-Sa1, BR-Sa3, and GF-Guy) located in Amazonian forests (red dots in fig. S1A and table S1) and acquired the data from the FLUXNET2015 TIER ONE dataset (*59*). We picked up half-hourly or hourly GPP, LE, shortwave radiation (Rg), and VPD and removed low-quality data using quality control flag. The clearness index, which is the ratio of shortwave radiation to potential radiation at the top of the atmosphere, was calculated to remove data collected under cloudy skies (clearness index < 0.3). GPP-based WUE (WUE_{GPP}) was calculated as the ratio of GPP to LE. The local time was converted to local solar time based on the time zone and longitude to enable comparisons with data acquired by the OCO-3 and ECOSTRESS instruments. All data for the available period were averaged into hourly data from 7:00 to 17:00 and per month to represent the climatology.

RF model

The available OCO-3 SIF and ECOSTRESS ET data were sparse in time and space and had substantial gaps (figs. S17 and S18) due to the high cloud cover over the study region and the ISS orbit. Discrete sampling of SIF and ET might produce biased diurnal patterns and spatial distributions after simple aggregation if data are not properly processed. However, the thousands of satellite-based SIF and ET data points we acquired were sufficient to train a machine learning model, such as the RF model (*60*). RF models can represent the nonlinear interactions among various variables and are relatively insensitive to outliers. Accordingly, we used RF models to generate temporally and spatially continuous SIF and ET fields. OCO-3 SIF and ECOSTRESS ET are released at different spatial resolutions. To maintain consistency, we averaged instantaneous OCO-3 SIF and ECOSTRESS ET into 0.1° × 0.1° grids and then used the gridded SIF and ET as response variables in the RF model. FPAR derived from Copernicus LAI and clear-sky DSSR, T_{air}, VPD, and SM from the ERA5 reanalyzed data were used as predictor variables. Note that SM was 0- to 100-cm volumetric SM, which was weighted average from three levels of ERA5 SM (0 to 7, 7 to 28, and 28 to 100 cm) according to their respective depth.

Because of the hysteretic and asymmetric responses of photosynthesis and ET to environmental drivers, particularly between morning and afternoon (*15*), we trained the RF model individually for the wet season morning, wet season afternoon, dry season morning, and dry season afternoon. Precipitation was used to define the wet and dry seasons at the grid cell level in each month (fig. S19): Months with precipitation rates higher than the annual mean were defined as the wet season, and months with precipitation rates lower than the annual mean were defined as the dry season (*33*). For the whole Amazon forest, the dry season was defined from June to October when >50% grid cells were in the dry season. The 100 RF models were used to predict SIF and ET in 1-hour intervals each month from 2015 to 2021 at a spatial resolution of 1° × 1°. The RF-based SIF and ET values were averaged to represent the climatological values over 2015–2021 without the interannual variations. The climatological SIF and ET values in the grid cells where the three ground flux sites (BR-Sa1, BR-Sa3, and GF-Guy) were located were compared with the tower GPP and ET data averaged from multiple years. The RF-based SIF and ET were well correlated with the GPP and ET data from the towers, with the correlation (r) of 0.86 and 0.92, respectively (fig. S20, A and B). Although the magnitude of RF-based ET was higher, such a bias had little effect on the diurnal trends or interannual trends expressed as percentages (%). The GPP-based WUE (WUE_{GPP} = GPP/LE) was also moderately correlated with the SIF-based WUE (WUE_{SIF} = SIF/ET) (R^2 = 0.44; fig. S20C). These results supported the use of RF-based SIF and ET for the diurnal and regional analysis of carbon and water fluxes. The interpolation and spatial and temporal extrapolation abilities of the RF models were evaluated in text S1. Only a small absolute relative bias (|rBias| < 0.2%) was observed for interpolation ability of RF models (fig. S21). In addition, the |rBias| was less than 0.8% for most cases in terms of spatial (fig. S22) and temporal extrapolation (fig. S23). We used the changes in SIF, ET, and WUE_{SIF} from morning to afternoon as the diurnal variations and from wet to dry season as the seasonal variations (Fig. 2).

Sensitivity analysis

The RF model was also used to calculate the sensitivities of SIF, ET, and WUE_{SIF} to perturbations in T_{air}, VPD, and SM, separately. We use the calculation of the sensitivity of ET to VPD as an example below. On the basis of the trained RF model described above, the FPAR and ERA-5 climatic data were used to produce ET (denoted as ET_O). Then, we produced ET (denoted ET_{VPD}) again by artificially adding one standard deviation to VPD, representing a disturbance, while keeping the other variables unchanged (*33*). Last, the sensitivity of ET to the disturbance in VPD was calculated using Eq. 6. The process was repeated using 100 RF models, and the means were analyzed to increase the robustness of the results (Figs. 6 and 7 and fig. S11). We also calculated the sensitivity of SIF and ET

to T_{air} by adding one SD and to SM by decreasing one SD.

$$\text{Sens.(ET) to VPD} = \text{mean}\left[\frac{\text{ET}_{\text{VPD}} - \text{ET}_{\text{O}}}{\text{ET}_{\text{O}}}\right] \times 100\% \quad (6)$$

Comparison of model$_{AM}$ + condition$_{AM}$ and model$_{PM}$ + condition$_{AM}$ simulations

The foliar water potential decreases from morning to afternoon due to the loss of water and then recovers during nighttime (*17*–*19*). To evaluate the afternoon reductions in photosynthesis and ET in response to the drop in foliar water potential and increases in T_{air} and VPD, we performed the model$_{AM}$ + condition$_{AM}$ and model$_{PM}$ + condition$_{AM}$ simulations, in which the morning and afternoon RF models were driven using the same morning inputs (including radiation, FPAR, T_{air}, VPD, and SM), respectively. By using the same morning inputs for both the morning and afternoon RF models, the effects of varying environmental drivers between morning and afternoon can be factored out. As an example, Eq. 7 was used to calculate the percentage change in ET from the model$_{AM}$ + condition$_{AM}$ simulations to the model$_{PM}$ + condition$_{AM}$ simulations

$$\text{Change in ET (\%)} = \frac{\text{ET}_{\text{PM}} - \text{ET}_{\text{AM}}}{\text{ET}_{\text{AM}}} \times 100\% \quad (7)$$

where ET$_{AM}$ and ET$_{PM}$ are the predicted ET using the model$_{AM}$ + condition$_{AM}$ and model$_{PM}$ + condition$_{AM}$ simulations, respectively.

Projection of photosynthesis and ET

The RF-based SIF and ET models were also used to predict diurnal SIF and ET from 2015 to 2100 under different combined SSPs and representative concentration pathways, including SSP245, SSP370, and SSP585, from CMIP6 (*36*). The climatic data (T_{air}, SM, specific humidity, surface pressure, and clear-sky radiation) with a 3-hour interval from CMIP6 models were resampled to hourly values (CMIP6 models can be found in table S2). T_{air}, specific humidity, and surface pressure were used to calculate VPD. Changing species composition could have a large impact on SIF and ET but is beyond the scope of this study and thus is not considered here. FPAR was kept constant at the values observed in 2015. Then, the hourly climatic data and FPAR were used in the trained RF model to simulate hourly SIF and ET. We analyzed relative changes in morning (7:00 to 12:00) and afternoon (12:00 to 17:00) SIF and ET from 2015 to 2100 across the Amazon forest. The morning and afternoon SIF and ET were averaged as daily averages, which were also compared with daily averaged GPP and ET predicted by CMIP6 models (see table S2) These comparisons will improve our understanding of the differences in photosynthesis and ET between satellite observation-based and model-based simulations. In addition, we used different datasets of training (mimicking the current conditions) and validation (mimicking the extrapolation to future higher VPD conditions than those used for calibration) to assess the uncertainty of RF models when making predictions of future scenarios (text S1 and fig. S24). Under the future conditions of SSP245 and SSP370, the |rBias| was less than 2% in all cases (figs. S25 and S26). Under the future conditions of SSP585, the highest |rBias| (4.03%; fig. S27E) was obtained for predicting ET in the wet season morning, followed by the dry season afternoon with the |rBias| of 3.17% (fig. S27H). In other cases, the |rBias| was less than 2% (fig. S27). Overall, these results indicate that the limited biases related to the future extrapolations would not affect our results and conclusions using RF models.

Supplementary Materials

This PDF file includes:

Tables S1 to S3
Figs. S1 to S27
Text S1

REFERENCES AND NOTES

1. W. Yuan, Y. Zheng, S. Piao, P. Ciais, D. Lombardozzi, Y. Wang, S. Yang, Increased atmospheric vapor pressure deficit reduces global vegetation growth. *Sci. Adv.* **5**, eaax1396 (2019).
2. N. McDowell, C. D. Allen, K. Anderson-Teixeira, P. Brando, R. Brienen, J. Chambers, B. Christoffersen, S. Davies, C. Doughty, A. Duque, F. Espirito-Santo, R. Fisher, C. G. Fontes, D. Galbraith, D. Goodsman, C. Grossiord, H. Hartmann, J. Holm, D. J. Johnson, A. R. Kassim, M. Keller, C. Koven, L. Kueppers, T. Kumagai, Y. Malhi, S. M. McMahon, M. Mencuccini, P. Meir, P. Moorcroft, H. C. Muller-Landau, O. L. Phillips, T. Powell, C. A. Sierra, J. Sperry, J. Warren, C. Xu, X. Xu, Drivers and mechanisms of tree mortality in moist tropical forests. *New Phytol.* **219**, 851–869 (2018).
3. B. E. Medlyn, E. Dreyer, D. Ellsworth, M. Forstreuter, P. C. Harley, M. U. F. Kirschbaum, D. Loustau, Temperature response of parameters of a biochemically based model of photosynthesis. II. A review of experimental data. *Plant Cell Environ.* **25**, 1167–1179 (2002).
4. A. Staal, O. A. Tuinenburg, J. H. C. Bosmans, M. Holmgren, E. H. van Nes, M. Scheffer, S. C. Dekker, Forest-rainfall cascades buffer against drought across the Amazon. *Nat. Clim. Chang.* **8**, 539–543 (2018).
5. D. C. Nepstad, I. M. Tohver, D. Ray, P. Moutinho, G. Cardinot, Mortality of large trees and lianas following experimental drought in an Amazon forest. *Ecology* **88**, 2259–2269 (2007).
6. V. A. Maia, A. B. M. Santos, N. de Aguiar-Campos, C. R. de Souza, M. C. F. de Oliveira, P. A. Coelho, R. M. dos Santos, The carbon sink of tropical seasonal forests in southeastern Brazil can be under threat. *Sci. Adv.* **6**, eabd4548 (2020).
7. R. R. Nemani, C. D. Keeling, H. Hashimoto, W. M. Jolly, S. C. Piper, C. J. Tucker, S. W. Running, Climate-driven increases in global terrestrial net primary production from 1982 to 1999. *Science* **300**, 1560–1563 (2003).
8. P. Gentine, J. K. Green, M. Guérin, V. Humphrey, S. I. Seneviratne, Y. Zhang, S. Zhou, Coupling between the terrestrial carbon and water cycles—A review. *Environ. Res. Lett.* **14**, 083003 (2019).
9. N. Restrepo-Coupe, N. M. Levine, B. O. Christoffersen, L. P. Albert, J. Wu, M. H. Costa, S. R. Saleska, Do dynamic global vegetation models capture the seasonality of carbon fluxes in the Amazon basin? A data-model intercomparison. *Glob. Chang. Biol.* **23**, 191–208 (2017).
10. A. M. Matheny, G. Bohrer, P. C. Stoy, I. T. Baker, A. T. Black, A. R. Desai, H. Verbeeck, Characterizing the diurnal patterns of errors in the prediction of evapotranspiration by several land-surface models: An NACP analysis. *Eur. J. Vasc. Endovasc. Surg.* **119**, 1458–1473 (2014).
11. J. Wu, L. P. Albert, A. P. Lopes, N. Restrepo-Coupe, M. Hayek, K. T. Wiedemann, N. Prohaska, Leaf development and demography explain photosynthetic seasonality in Amazon evergreen forests. *Science* **351**, 972–976 (2016).
12. N. Restrepo-Coupe, H. R. da Rocha, L. R. Hutyra, A. C. da Araujo, L. S. Borma, B. Christoffersen, S. R. Saleska, What drives the seasonality of photosynthesis across the Amazon basin? A cross-site analysis of eddy flux tower measurements from the Brasil flux network. *Agric. For. Meteorol.* **182-183**, 128–144 (2013).
13. C. von Randow, A. O. Manzi, B. Kruijt, P. J. de Oliveira, F. B. Zanchi, R. L. Silva, P. Kabat, Comparative measurements and seasonal variations in energy and carbon exchange over forest and pasture in South West Amazonia. *Theor. Appl. Climatol.* **78**, 5–26 (2004).
14. J. Wu, K. Guan, M. Hayek, N. Restrepo-Coupe, K. T. Wiedemann, X. Xu, S. R. Saleska, Partitioning controls on Amazon forest photosynthesis between environmental and biotic factors at hourly to interannual timescales. *Glob. Chang. Biol.* **23**, 1240–1257 (2017).
15. C. Lin, P. Gentine, C. Frankenberg, S. Zhou, D. Kennedy, X. Li, Evaluation and mechanism exploration of the diurnal hysteresis of ecosystem fluxes. *Agric. For. Meteorol.* **278**, 107642 (2019).
16. M. L. Goulden, S. D. Miller, H. R. da Rocha, M. C. Menton, H. C. de Freitas, A. M. e Silva Figueira, C. A. D. de Sousa, Diel and seasonal patterns of tropical forest CO_2 exchange. *Ecol. Appl.* **14**, 42–54 (2004).

17. J.-E. Lee, R. S. Oliveira, T. E. Dawson, I. Fung, Root functioning modifies seasonal climate. *Proc. Natl. Acad. Sci. U.S.A.* **102**, 17576–17581 (2005).
18. R. S. Oliveira, T. E. Dawson, S. S. O. Burgess, D. C. Nepstad, Hydraulic redistribution in three Amazonian trees. *Oecologia* **145**, 354–363 (2005).
19. R. B. Neumann, Z. G. Cardon, The magnitude of hydraulic redistribution by plant roots: A review and synthesis of empirical and modeling studies. *New Phytol.* **194**, 337–352 (2012).
20. A. R. Huete, K. Didan, Y. E. Shimabukuro, P. Ratana, S. R. Saleska, L. R. Hutyra, R. Myneni, Amazon rainforests green-up with sunlight in dry season. *Geophys. Res. Lett.* **33**, L06405 (2006).
21. E. N. Stavros, D. Schimel, R. Pavlick, S. Serbin, A. Swann, L. Duncanson, P. Wennberg, ISS observations offer insights into plant function. *Nat. Ecol. Evol.* **1**, 0194 (2017).
22. J. B. Fisher, B. Lee, A. J. Purdy, G. H. Halverson, M. B. Dohlen, K. Cawse-Nicholson, S. Hook, ECOSTRESS: NASA's next generation mission to measure evapotranspiration from the international space station. *Water Resources Res.* **56**, e2019WR026058 (2020).
23. T. E. Taylor, A. Eldering, A. Merrelli, M. Kiel, P. Somkuti, C. Cheng, S. Yu, OCO-3 early mission operations and initial (vEarly) XCO_2 and SIF retrievals. *Remote Sens. Environ.* **251**, 112032 (2020).
24. M. Meroni, M. Rossini, L. Guanter, L. Alonso, U. Rascher, R. Colombo, J. Moreno, Remote sensing of solar-induced chlorophyll fluorescence: Review of methods and applications. *Remote Sens. Environ.* **113**, 2037–2051 (2009).
25. C. Frankenberg, J. B. Fisher, J. Worden, G. Badgley, S. S. Saatchi, J. E. Lee, A. Kuze, New global observations of the terrestrial carbon cycle from GOSAT: Patterns of plant fluorescence with gross primary productivity. *Geophys. Res. Lett.* **38**, 351–365 (2011).
26. J. Joiner, Y. Yoshida, A. P. Vasilkov, Y. Yoshida, L. A. Corp, E. M. Middleton, First observations of global and seasonal terrestrial chlorophyll fluorescence from space. *Biogeosciences* **8**, 637–651 (2011).
27. Y. Sun, C. Frankenberg, J. D. Wood, D. S. Schimel, M. Jung, L. Guanter, T. J. Griffis, L. Gu, T. S. Magney, P. Köhler, B. Evans, K. Yuen, OCO-2 advances photosynthesis observation from space via solar-induced chlorophyll fluorescence. *Science* **358**, eaam5747 (2017).
28. X. Li, J. Xiao, B. He, M. A. Arain, J. Beringer, A. R. Desai, A. Varlagin, Solar-induced chlorophyll fluorescence is strongly correlated with terrestrial photosynthesis for a wide variety of biomes: First global analysis based on OCO-2 and flux tower observations. *Glob. Chang. Biol.* **24**, 3990–4008 (2018).
29. R. Doughty, P. Köhler, C. Frankenberg, T. S. Magney, X. Xiao, Y. Qin, B. Moore III, TROPOMI reveals dry-season increase of solar-induced chlorophyll fluorescence in the Amazon forest. *Proc. Natl. Acad. Sci. U.S.A.* **116**, 22393–22398 (2019).
30. N. C. Parazoo, K. Bowman, C. Frankenberg, J. E. Lee, J. B. Fisher, J. Worden, I. T. Baker, Interpreting seasonal changes in the carbon balance of southern Amazonia using measurements of XCO_2 and chlorophyll fluorescence from GOSAT. *Geophys. Res. Lett.* **40**, 2829–2833 (2013).
31. J. E. Lee, C. Frankenberg, C. van der Tol, J. A. Berry, L. Guanter, C. K. Boyce, S. Saatchi, Forest productivity and water stress in Amazonia: Observations from GOSAT chlorophyll fluorescence. *Proc. R. Soc. Lond. B Biol. Sci.* **280**, 20130171 (2013).
32. A. O. Castro, J. Chen, C. S. Zang, A. Shekhar, J. C. Jimenez, S. Bhattacharjee, A. Rammig, OCO-2 solar-induced chlorophyll fluorescence variability across ecoregions of the Amazon basin and the extreme drought effects of El Niño (2015–2016). *Remote Sens* **12**, 1202 (2020).
33. J. K. Green, J. Berry, P. Ciais, Y. Zhang, P. Gentine, Amazon rainforest photosynthesis increases in response to atmospheric dryness. *Sci. Adv.* **6**, eabb7232 (2020).
34. J. Xiao, J. B. Fisher, H. Hashimoto, K. Ichii, N. C. Parazoo, Emerging satellite observations for diurnal cycling of ecosystem processes. *Nat. Plants* **7**, 877–887 (2021).
35. M. Huang, S. Piao, Z. Zeng, S. Peng, P. Ciais, L. Cheng, Y. Wang, Seasonal responses of terrestrial ecosystem water-use efficiency to climate change. *Glob. Chang. Biol.* **22**, 2165–2177 (2016).
36. B. C. O'Neill, C. Tebaldi, D. P. van Vuuren, V. Eyring, P. Friedlingstein, G. Hurtt, B. M. Sanderson, The scenario model intercomparison project (ScenarioMIP) for CMIP6. *Geosci. Model Dev.* **9**, 3461–3482 (2016).
37. C. P. Bickford, D. T. Hanson, N. G. McDowell, Influence of diurnal variation in mesophyll conductance on modelled 13C discrimination: Results from a field study. *J. Exp. Bot.* **61**, 3223–3233 (2010).
38. L. D. Prior, D. Eamus, G. A. Duff, Seasonal trends in carbon assimilation, stomatal conductance, pre-dawn leaf water potential and growth in *Terminalia ferdinandiana*, a deciduous tree of northern Australian savannas. *Aust. J. Bot.* **45**, 53–69 (1997).
39. A. Massmann, P. Gentine, C. Lin, When does vapor pressure deficit drive or reduce evapotranspiration? *J. Adv. Model. Earth Syst* **11**, 3305–3320 (2019).
40. M. Ishibashi, I. Terashima, Effects of continuous leaf wetness on photosynthesis: Adverse aspects of rainfall. *Plant Cell Environ.* **18**, 431–438 (1995).
41. U. Anber, P. Gentine, S. Wang, A. H. Sobel, Fog and rain in the Amazon. *Proc. Natl. Acad. Sci. U.S.A.* **112**, 11473–11477 (2015).
42. M. Slot, K. Winter, In situ temperature response of photosynthesis of 42 tree and liana species in the canopy of two Panamanian lowland tropical forests with contrasting rainfall regimes. *New Phytol.* **214**, 1103–1117 (2017).
43. J. Joiner, Y. Yoshida, A. P. Vasilkov, K. Schaefer, M. Jung, L. Guanter, L. Belelli Marchesini, The seasonal cycle of satellite chlorophyll fluorescence observations and its relationship to vegetation phenology and ecosystem atmosphere carbon exchange. *Remote Sens. Environ.* **152**, 375–391 (2014).
44. C. Grossiord, T. N. Buckley, L. A. Cernusak, K. A. Novick, B. Poulter, R. T. W. Siegwolf, N. G. McDowell, Plant responses to rising vapor pressure deficit. *New Phytol.* **226**, 1550–1566 (2020).
45. G. B. Bonan, Forests and climate change: Forcings, feedbacks, and the climate benefits of forests. *Science* **320**, 1444–1449 (2008).
46. B. E. Medlyn, R. A. Duursma, D. Eamus, D. S. Ellsworth, I. C. Prentice, C. V. M. Barton, L. Wingate, Reconciling the optimal and empirical approaches to modelling stomatal conductance. *Glob. Chang. Biol.* **17**, 2134–2144 (2011).
47. J. E. Drake, M. G. Tjoelker, A. Vårhammar, B. E. Medlyn, P. B. Reich, A. Leigh, C. V. M. Barton, Trees tolerate an extreme heatwave via sustained transpirational cooling and increased leaf thermal tolerance. *Glob. Chang. Biol.* **24**, 2390–2402 (2018).
48. Q. Quan, D. Tian, Y. Luo, F. Zhang, T. W. Crowther, K. Zhu, S. Niu, Water scaling of ecosystem carbon cycle feedback to climate warming. *Sci. Adv.* **5**, eaav1131 (2019).
49. G. R. Quetin, A. L. S. Swann, Empirically derived sensitivity of vegetation to climate across global gradients of temperature and precipitation. *J. Climate* **30**, 5835–5849 (2017).
50. K. A. Novick, D. L. Ficklin, P. C. Stoy, C. A. Williams, G. Bohrer, A. C. Oishi, R. P. Phillips, The increasing importance of atmospheric demand for ecosystem water and carbon fluxes. *Nat. Clim. Chang.* **6**, 1023–1027 (2016).
51. R. Doughty, T. P. Kurosu, N. Parazoo, P. Köhler, Y. Wang, Y. Sun, C. Frankenberg, Global GOSAT, OCO-2, and OCO-3 solar-induced chlorophyll fluorescence datasets. *Earth Syst. Sci. Data* **14**, 1513–1529 (2022).
52. Z. Y. Zhang, Y. G. Zhang, A. Porcar-Castell, J. Joiner, L. Guanter, X. Yang, Y. Goulas, Reduction of structural impacts and distinction of photosynthetic pathways in a global estimation of GPP from space-borne solar-induced chlorophyll fluorescence. *Remote Sens. Environ.* **240**, 111722 (2020).
53. Z. Zhang, Y. Zhang, Solar angle matters: Diurnal pattern of solar-induced chlorophyll fluorescence from OCO-3 and TROPOMI. *Remote Sens. Environ.* **285**, 113380 (2023).
54. X. Liu, L. Liu, J. Hu, J. Guo, S. Du, Improving the potential of red SIF for estimating GPP by downscaling from the canopy level to the photosystem level. *Agric. For. Meteorol.* **281**, 107846 (2020).
55. J. B. Fisher, K. P. Tu, D. D. Baldocchi, Global estimates of the land–atmosphere water flux based on monthly AVHRR and ISLSCP-II data, validated at 16 FLUXNET sites. *Remote Sens. Environ.* **112**, 901–919 (2008).
56. S. P. Good, D. Noone, G. Bowen, Hydrologic connectivity constrains partitioning of global terrestrial water fluxes. *Science* **349**, 175–177 (2015).
57. J. M. Chen, J. Liu, S. G. Leblanc, R. Lacaze, J.-L. Roujean, Multi-angular optical remote sensing for assessing vegetation structure and carbon absorption. *Remote Sens. Environ.* **84**, 516–525 (2003).
58. A. Barkhordarian, S. S. Saatchi, A. Behrangi, P. C. Loikith, C. R. Mechoso, A recent systematic increase in vapor pressure deficit over tropical south America. *Sci. Rep.* **9**, 15331 (2019).
59. G. Pastorello, C. Trotta, E. Canfora, H. Chu, D. Christianson, Y.-W. Cheah, C. Poindexter, J. Chen, A. Elbashandy, M. Humphrey, P. Isaac, D. Polidori, M. Reichstein, A. Ribeca, C. van Ingen, N. Vuichard, L. Zhang, B. Amiro, C. Ammann, M. A. Arain, J. Ardö, T. Arkebauer, S. K. Arndt, N. Arriga, M. Aubinet, M. Aurela, D. Baldocchi, A. Barr, E. Beamesderfer, L. B. Marchesini, O. Bergeron, J. Beringer, C. Bernhofer, D. Berveiller, D. Billesbach, T. A. Black, P. D. Blanken, G. Bohrer, J. Boike, P. V. Bolstad, D. Bonal, J.-M. Bonnefond, D. R. Bowling, R. Bracho, J. Brodeur, C. Brümmer, N. Buchmann, B. Burban, S. P. Burns, P. Buysse, P. Cale, M. Cavagna, P. Cellier, S. Chen, I. Chini, T. R. Christensen, J. Cleverly, A. Collalti, C. Consalvo, B. D. Cook, D. Cook, C. Coursolle, E. Cremonese, P. S. Curtis, E. D'Andrea, H. da Rocha, X. Dai, K. J. Davis, B. De Cinti, A. de Grandcourt, A. De Ligne, R. C. De Oliveira, N. Delpierre, A. R. Desai, C. M. Di Bella, P. di Tommasi, H. Dolman, F. Domingo, G. Dong, S. Dore, P. Duce, E. Dufrêne, A. Dunn, J. Dušek, D. Eamus, U. Eichelmann, H. A. M. El Khidir, W. Eugster, C. M. Ewenz, B. Ewers, D. Famulari, S. Fares, I. Feigenwinter, A. Feitz, R. Fensholt, G. Filippa, M. Fischer, J. Frank, M. Galvagno, M. Gharun, D. Gianelle, B. Gielen, B. Gioli, A. Gitelson, I. Goded, M. Goeckede, A. H. Goldstein, C. M. Gough, M. L. Goulden, A. Graf, A. Griebel, C. Gruening, T. Grünwald, A. Hammerle, S. Han, X. Han, B. U. Hansen, C. Hanson, J. Hatakka, Y. He, M. Hehn, B. Heinesch, N. Hinko-Najera, L. Hörtnagl, L. Hutley, A. Ibrom, H. Ikawa, M. Jackowicz-Korczynski, D. Janouš, W. Jans, R. Jassal, S. Jiang, T. Kato, M. Khomik, J. Klatt, A. Knohl, S. Knox, H. Kobayashi, G. Koerber, O. Kolle, Y. Kosugi, A. Kotani, A. Kowalski, B. Kruijt, J. Kurbatova, W. L. Kutsch, H. Kwon, S. Launiainen, T. Laurila, B. Law, R. Leuning, Y. Li, M. Liddell, J.-M. Limousin, M. Lion, A. J. Liska, A. Lohila, A. López-Ballesteros, E. López-Blanco, B. Loubet, D. Loustau, A. Lucas-Moffat, J. Lüers, S. Ma, C. Macfarlane, V. Magliulo, R. Maier, I. Mammarella, G. Manca, B. Marcolla, H. A. Margolis, S. Marras, W. Massman,

M. Mastepanov, R. Matamala, J. H. Matthes, F. Mazzenga, H. M. Caughey, I. M. Hugh, A. M. S. McMillan, L. Merbold, W. Meyer, T. Meyers, S. D. Miller, S. Minerbi, U. Moderow, R. K. Monson, L. Montagnani, C. E. Moore, E. Moors, V. Moreaux, C. Moureaux, J. W. Munger, T. Nakai, J. Neirynck, Z. Nesic, G. Nicolini, A. Noormets, M. Northwood, M. Nosetto, Y. Nouvellon, K. Novick, W. Oechel, J. E. Olesen, J.-M. Ourcival, S. A. Papuga, F.-J. Parmentier, E. Paul-Limoges, M. Pavelka, M. Peichl, E. Pendall, R. P. Phillips, K. Pilegaard, N. Pirk, G. Posse, T. Powell, H. Prasse, S. M. Prober, S. Rambal, Ü. Rannik, N. Raz-Yaseef, C. Rebmann, D. Reed, V. R. de Dios, N. Restrepo-Coupe, B. R. Reverter, M. Roland, S. Sabbatini, T. Sachs, S. R. Saleska, E. P. Sánchez-Cañete, Z. M. Sanchez-Mejia, H. P. Schmid, M. Schmidt, K. Schneider, F. Schrader, I. Schroder, R. L. Scott, P. Sedlák, P. Serrano-Ortíz, C. Shao, P. Shi, I. Shironya, L. Siebicke, L. Šigut, R. Silberstein, C. Sirca, D. Spano, R. Steinbrecher, R. M. Stevens, C. Sturtevant, A. Suyker, T. Tagesson, S. Takanashi, Y. Tang, N. Tapper, J. Thom, M. Tomassucci, J.-P. Tuovinen, S. Urbanski, R. Valentini, M. van der Molen, E. van Gorsel, K. van Huissteden, A. Varlagin, J. Verfaillie, T. Vesala, C. Vincke, D. Vitale, N. Vygodskaya, J. P. Walker, E. Walter-Shea, H. Wang, R. Weber, S. Westermann, C. Wille, S. Wofsy, G. Wohlfahrt, S. Wolf, W. Woodgate, Y. Li, R. Zampedri, J. Zhang, G. Zhou, D. Zona, D. Agarwal, S. Biraud, M. Torn, D. Papale, The FLUXNET2015 dataset and the ONEFlux processing pipeline for eddy covariance data. *Sci. Data* **7**, 225 (2020).

60. L. Breiman, Random Forests. *Mach. Learn.* **45**, 5–32 (2001).

Acknowledgments

Funding: This research was supported by the National Natural Science Foundation of China (42125105, 42071388, and 42101320). J.W. was in part funded by National Natural Science Foundation of China (31922090) and in part supported by the Innovation and Technology Fund (funding support to State Key Laboratories in Hong Kong of Agrobiotechnology) of the Hong Kong Special Administrative Region, China. P.G. acknowledges funding from USMILE European Research Council grant. S. R. Saleska and N. Restrepo-Coupe were appreciated for providing flux data. **Author contributions:** Z.Z. and Y.Z. conceived the study. Z.Z., Y.Z., A.C., Y.-P.W., P.G., and J.X. contributed to interpreting the results. All authors edited the manuscript. **Competing interests:** The authors declare that they have no competing interests. **Data and materials availability:** All data needed to evaluate the conclusions in the paper are present in the paper and/or the Supplementary Materials. Details about CMIP6 models used in this study are provided in table S2. The data used in this study have been properly cited and are publicly available (see table S3).

Submitted 15 April 2022
Accepted 25 April 2023
Published 26 May 2023
10.1126/sciadv.abq4974